Article

Porous Metal−Organic Polyhedra: Morphology, Porosity, and Guest Binding

Stephen P. Argent,* Ivan da Silva, Alex Greenaway, Mathew Savage, Jack Humby, Andrew J. Davies, Harriott Nowell, William Lewis, Pascal Manuel, Chiu C. Tang, Alexander J. Blake, Michael W. George, Alexander V. Markevich, Elena Besley, Sihai Yang, Neil R. Champness,* and Martin Schröder*

Read Online

ACCESS | Metrics & More | Article Recommendations | SI Supporting Information

ABSTRACT: Designing porous materials which can selectively adsorb CO_2 or CH_4 is an important environmental and industrial goal which requires an understanding of the host−guest interactions involved at the atomic scale. Metal−organic polyhedra (MOPs) showing permanent porosity upon desolvation are rarely observed. We report a family of MOPs (**Cu-1a**, **Cu-1b**, **Cu-2**), which derive their permanent porosity from cavities between packed cages rather than from within the polyhedra. Thus, for **Cu-1a**, the void fraction outside the cages totals 56% with only 2% within. The relative stabilities of these MOP structures are rationalized by considering their weak nondirectional packing interactions using Hirshfeld surface analyses. The exceptional stability of **Cu-1a** enables a detailed structural investigation into the adsorption of CO_2 and CH_4 using *in situ* X-ray and neutron diffraction, coupled with DFT calculations. The primary binding sites for adsorbed CO_2 and CH_4 in **Cu-1a** are found to be the open metal sites and pockets defined by the faces of phenyl rings. More importantly, the structural analysis of a hydrated sample of **Cu-1a** reveals a strong hydrogen bond between the adsorbed CO_2 molecule and the Cu(II)-bound water molecule, shedding light on previous empirical and theoretical observations that partial hydration of metal−organic framework (MOF) materials containing open metal sites increases their uptake of CO_2. The results of the crystallographic study on MOP−gas binding have been rationalized using DFT calculations, yielding individual binding energies for the various pore environments of **Cu-1a**.
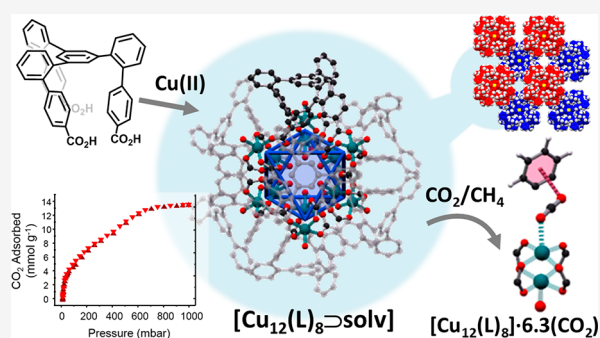
INTRODUCTION

Porous materials such as metal−organic frameworks (MOFs),[1] covalent organic frameworks (COFs),[2] porous organic polymers,[3] and porous molecular solids[4] have been investigated for a wide range of applications, including gas adsorption and separation, conductivity, photochemistry, and catalysis. Each class of materials possesses both strengths and weaknesses in terms of their properties and function such as adsorption capacity, selectivity, tunability, stability, and processability.[5] A detailed understanding of the interactions between guest molecules and the host material is of critical importance to the design of improved functional materials, and *in situ* diffraction methods have made significant advances in delivering detailed structural insights into host−guest binding interactions in MOFs and porous molecular solids.[6] In contrast, far fewer examples have been reported of permanently porous materials derived from metal−organic polyhedra (MOPs),[7] and many show weak intermolecular forces leading to structural collapse upon desolvation.[7g,8]

MOPs are derived from polytopic ligands that bridge metal cations or clusters to give discrete molecular species, often with highly symmetrical architectures.[9] Porosity in MOPs can originate either from the space inside the polyhedral cages or from the spaces between cages when they pack in the solid state to form 3D structures.[10] Control over the former can be achieved by targeting specific polyhedral topologies and shapes through the combination of appropriate rigid organic linkers and metal centers.[11] Control over the latter is much harder because the assembly of MOPs is directed by poorly directional weak interactions and is thus often unpredictable. More significantly, the tendency to maximize the number of weak contacts during crystallization tends to favor more dense nonporous phases.[12] The formation of a MOP material with permanent porosity therefore requires a rigid MOP assembly which can frustrate efficient packing and resist structural collapse upon desolvation, a combination that is rarely observed. Porous organic molecular materials have been
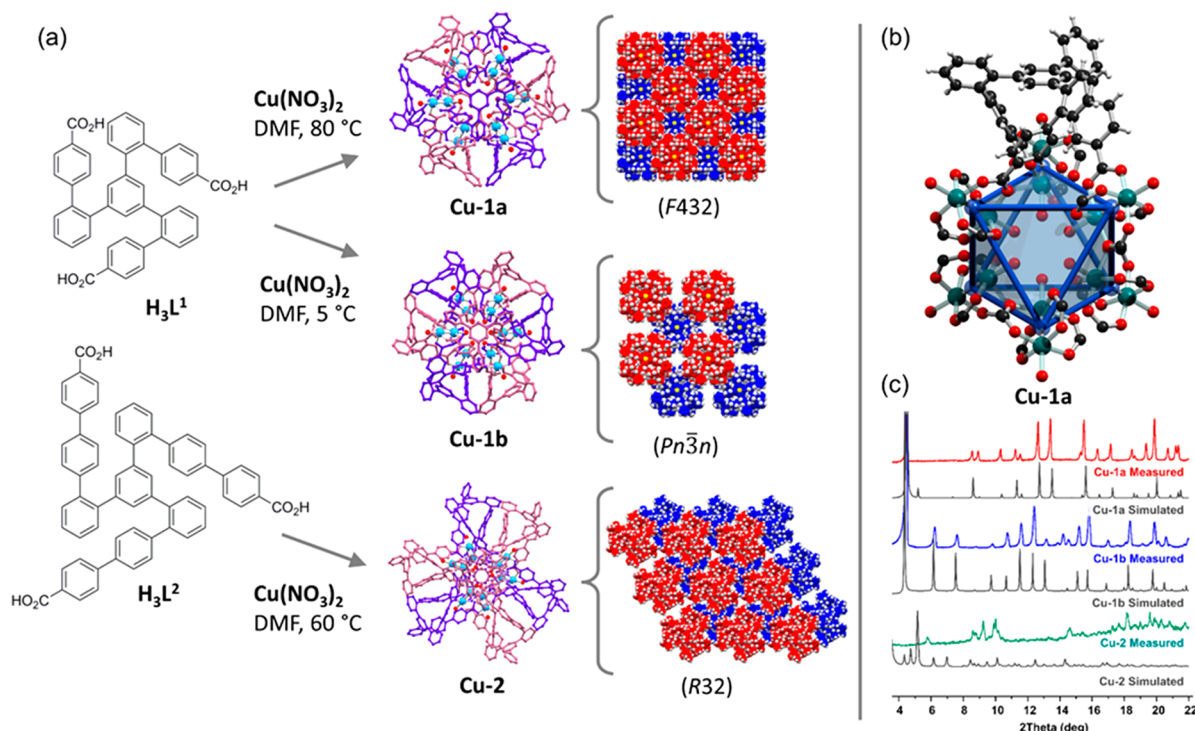
Figure 1. (a) Synthesis of metal−organic porous materials **Cu-1a**, **Cu-1b**, and **Cu-2** by reaction of H_3L^1 and H_3L^2 with $Cu(NO_3)_2$. The space groups of their crystal structures are shown underneath the packing views. Molecular cage color code: copper, light blue; water, red; ligands, pink and purple; hydrogen atoms omitted. Crystal packing view color code: cages of alternating layers, red and blue; hydrogen atoms, white. (b) Conformation of $(L^1)^{3-}$ in **Cu-1a**. Eight tripodal ligands straddle a triangular face of the octahedral array of copper paddlewheel units (only one ligand is shown). Color code: copper, teal; carbon, black; oxygen, red; hydrogen, white; paddlewheel centroids and connecting edges, blue. (c) Comparisons of measured and simulated PXRD patterns for samples of **Cu-1a**, **Cu-1b** and **Cu-2**. Simulated patterns are generated from the single crystal X-ray diffraction (SCXRD) structures. The measured powder X-ray diffraction (PXRD) pattern of **Cu-2** after solvent exchange shows differences from the pattern calculated from the solvated form, indicating some rearrangement of the structure upon loss of solvent.

demonstrated previously by the self-assembly of imines[13] and cyclic boronate ester[14] cages. Here, we report the synthesis of a family of isotopological Cu(II)-containing MOPs composed from tripodal tricarboxylic acids,[15] which assemble to give porous MOP materials denoted **Cu-1a**, **Cu-1b**, and **Cu-2**. Hirshfeld surface analyses of the cage molecules give insight into the origins of the stability and concomitant supramolecular interactions within this family of materials. An investigation of CO_2 and CH_4 adsorption in the most stable material, **Cu-1a**, confirms that these guest species have distinct preferences for binding sites. The combination of *in situ* diffraction experiments,[6a,16] IR spectroscopy,[17] and DFT calculations[18] delivers a comprehensive picture of the host−guest interactions in **Cu-1a**.

Porous materials able to selectively adsorb CO_2 over N_2 or CH_4 are candidates for applications in carbon capture[19] and biogas processing.[20] Strategies to enhance CO_2 adsorption in porous materials include the introduction of open metal sites[16d,21] and functional groups such as amines,[22] amides,[23] and hydroxyl moieties,[24] which can make strong and specific interactions with the quadrupolar adsorbate. Another practical method found to increase CO_2 uptake is partial hydration of framework materials leading to an increased strength of interaction between CO_2 and the coordinated water molecule on metal sites.[25] Herein we report structural evidence for the formation of hydrogen bonds between adsorbed CO_2 molecules and Cu(II)-bound water molecules, affording key structural evidence for previously reported observations.

■ EXPERIMENTAL DETAILS

Synthesis. H_3L^1 and H_3L^2 (Figure 1) were prepared according to literature methods.[15a,b]

Cu-1a. H_3L^1 (3.52 g, 5.29 mmol) and $Cu(NO_3)_2 \cdot 3H_2O$ (4.90 g, 21.1 mmol) were dissolved separately in portions of DMF before being combined in a round-bottom flask and diluted to a total volume of 530 mL. The solution was purged with N_2 for 30 min before being heated to 85 °C without stirring for 3 days. A fine pale blue precipitate gathered at the bottom of the flask was collected by filtration while the solution was still hot and washed with portions of hot DMF. A small number of large (up to 200 μm) fractal-fern-shaped crystals were formed, and these were collected and used for X-ray analysis. The powder was then solvent-exchanged with acetone by soaking the material under acetone, which was replaced daily for 7 days before the solid was dried under a gentle flow of Ar to give **Cu-1a** as a fine azure blue powder (yield 1.75 g, 38%). Anal. Calcd for $Cu_{12}(C_{45}H_{27}O_6)_8(H_2O)_{40}(C_3H_7NO)_3$: C, 66.93; H, 4.83; N, 0.62. Found: C, 66.63; H, 4.20; N, 0.63%. **Cu-1a** was treated in a Tousimis Autosamdri-815 Series A supercritical point dryer prior to further analysis: the acetone-exchanged material was suspended in EtOH before it was loaded into the dryer in a porous crucible. The EtOH was purged with CO_2 for 10 min before being allowed to equilibrate for 50 min. This process was repeated four times. The CO_2 was heated above the supercritical point before the pressure was slowly released over 3 h.

Cu-1b. H_3L^1 (2.01 g, 3.02 mmol) and $Cu(NO_3)_2 \cdot 3H_2O$ (2.35 g, 9.71 mmol) were separately dissolved in portions of DMF before being combined in a 1000 mL square Schott bottle and diluted to a total volume of 975 mL. The bottle was capped and chilled to 4 °C for 48 h, after which a fine pale blue precipitate had formed. A small number of large single crystals formed, and these were collected and used for X-ray analysis. The precipitate was collected by filtration and

washed sequentially with portions of DMF and acetone before being dried under a gentle flow of argon to give **Cu-1b** as a pale blue crystalline powder (yield 0.319 g, 10.5%). Anal. Calcd for $Cu_{12}(C_{45}H_{27}O_6)_8(H_2O)_{55}(C_3H_7NO)_{13}$: C, 60.48; H, 5.18; N, 2.30. Found: C, 59.81; H, 5.24; N, 2.27%. After the solution was left for a further 48 h, more blue precipitate formed; however, this material was shown by powder X-ray diffraction to have poorer crystallinity, as evidenced by broader peaks in the diffraction pattern. After the solution was left for 7 days more blue precipitate formed: this material was shown by powder X-ray diffraction to have broad peaks consistent with the structure of **Cu-1a**. Unreacted ligand H_3L^1 could be recovered from the reaction mixture by concentrating a DMF solution under reduced pressure before adding concentrated HCl to precipitate the ligand.

Cu-2. Ligand H_3L^2 (240 mg, 0.268 mmol) and $Cu(NO_3)_2\cdot3H_2O$ (259 mg, 1.071 mmol) were separately dissolved in portions of DMF before being combined in a round-bottom flask and diluted to a total volume of 25 mL. The solution was purged with N_2 for 30 min before being heated to 80 °C without stirring for 2 days, which resulted in the formation of large blue-green rhombus crystals. The solution was cooled before the crystals were collected by filtration and washed with portions of DMF. The crystals were then solvent-exchanged under ethanol, which was replaced daily for 1 week before being dried under a flow of N_2 to give **Cu-2** as a blue-green solid (yield 123 mg, 42.3%). Anal. Calcd for $Cu_{12}(C_{63}H_{39}O_6)_8(H_2O)_{55}$: C, 69.51; H, 4.65; N, 0.00. Found: C, 69.68; H, 4.66; N, 0.07%. The trace amounts of N in the sample reflect the presence of some residual dmf.

Where yields for complexation are given above, they are calculated for the formula weight of the solvated product indicated by elemental analysis.

Gas Adsorption. Gravimetric sorption isotherms for CO_2, CH_4, and H_2 were recorded at 77 K (liquid N_2), 87 K (liquid Ar), or 273−298 K (temperature-programmed water bath) using a Hiden Isochema IGA-003 system under ultrahigh vacuum from a diaphragm and turbo pumping system. All gases used were ultrapure research grade (99.999%) purchased from BOC or Air Liquide. In a typical gas adsorption experiment, 65 mg of acetone exchanged **Cu-1a** was loaded into an IGA and degassed at 160 °C under high vacuum (10^{-9} bar measured at pump) for 48 h to give desolvated **Cu-1a**. Volumetric sorption isotherms for N_2, CO_2, and CH_4 were recorded at 77 K (liquid N_2), 87 K (liquid Ar), or 195 K (dry ice acetone bath) using a Quantachrome Autosorb-1 or a Micromeritics 3Flex Surface Characterization Analyzer. BET surface areas and were calculated with the Micromeritics 3Flex software package, examining the Rouquerol-BET plot function to determine the optimum range of pressure in p/p_0.

IR Spectroscopy. *In situ* studies on **Cu-1a** were carried out in a high-pressure low-temperature cell, which has been described in detail elsewhere.[26] KBr disks with and without **Cu-1a** (ca. 5 mg) were used as the matrices for *in situ* IR experiments to record the spectra for the material and background, respectively. **Cu-1a** was pressed into the surface of a preformed KBr disk. The disks were further degassed by heating to 120 °C under high vacuum for 3 h and mounted into the cell, which was purged with Ar. The disk was placed under vacuum, cooled to 273 or 195 K, and filled to various pressures between 0 and 1 bar of CO_2 (CP grade, supplied by BOC) to mimic the gas sorption experiments. For each pressure step, the equilibration time was set to 30−60 min before the measurement of IR spectra. All IR spectra were recorded on a Nicolet Avatar 360 FTIR spectrometer with a liquid-nitrogen-cooled HgCdTe detector.

Single-Crystal X-ray Diffraction. Diffraction data for **Cu-1a** were collected at Diamond Light Source, Beamline I19, on a CrystalLogic Kappa 4-circle diffractometer equipped with a Rigaku Saturn 724+ CCD detector using synchrotron radiation with a wavelength of 0.6889 Å.[27] The raw data were reduced and corrected for Lorentz and polarization effects using CrystalClear[28] and corrected for the effects of adsorption using Scale implemented in CrystalClear. All structures were solved by direct methods (SHELXS)[7] and refined by full-matrix least squares (SHELXL).[29]

Regions of diffuse solvent in the solvated structures were treated with the PLATON SQUEEZE routine.[30]

Diffraction data for **Cu-1b** and **Cu-2** were collected on a Rigaku Oxford Diffraction SuperNova diffractometer equipped with an AtlasS2 detector and microfocus Cu X-ray source. Diffraction data for **Cu-1a·H₂O** and **Cu-1a·H₂O−CO₂** were collected on a Rigaku Oxford Diffraction SuperNova diffractometer equipped with a TitanS2 detector and microfocus Cu X-ray source. The raw data were reduced and corrected for Lorentz and polarization effects using CrysAlisPro;[31] corrections for the effects of adsorption were applied using a numerical absorption correction based on Gaussian integration over a multifaceted crystal model. For the *in situ* experiment a single crystal of **Cu-1a** was removed from the DMF reaction medium and dried with a MiTeGen liquid wick before being washed with fresh DMF and redried. The crystal was glued to a MiTeGen microgripper using a minimum of epoxy adhesive before being mounted inside a quartz capillary attached to a custom static gas cell. The cell was heated under vacuum (10^{-5} mbar measured at the pump) at 150 °C for 10 days before being cooled and sealed under vacuum. Diffraction data for the evacuated crystal were measured with the cell cooled by a Cryostream open-flow cryostat set at 220 K (this was the lowest temperature at which icing of the quartz capillary did not occur). The evacuated cell was then reconnected to vacuum and heated for a further 24 h before being cooled to room temperature and backfilled with CO_2 (1.5 bar). The cell was cooled to 100 K under the cryostream before the quartz sheath was rapidly removed, leaving the gas-loaded crystal to be rapidly frozen directly under a flow of N_2.

Neutron Powder Diffraction. *In situ* experiments were undertaken using the WISH diffractometer at the ISIS facility.[32] Acetone-exchanged **Cu-1a** was loaded into a 6 mm diameter vanadium sample can and placed under vacuum at 10^{-7} mbar and 100 °C for 3 days. The sample was loaded into a liquid-helium cryostat and cooled to 10 K for data collection of **Cu-1a**. The guest gases CO_2 and CD_4 were dosed volumetrically from a calibrated volume after the sample was warmed to 298 K (CO_2 dosing) or 150 K (CD_4 dosing) with measurements made for loadings of 6 and 18 molecules of CO_2 per Cu_{12} cage unit and 6 molecules of CD_4 per Cu_{12} cage unit. The sample was slowly cooled to 10 K to ensure that CO_2 and CD_4 were completely adsorbed with no condensation in the cell. Time was allowed to achieve thermal equilibrium before data collection. The locations of adsorbed CO_2 and CD_4 molecules were determined as a function of gas loading by sequential Fourier difference map analysis followed by Rietveld refinement using the TOPAS software package.[10] Analysis of the Fourier map of **Cu-1a** indicated no residual nuclear density in the large octahedral and small tetrahedral intermolecular voids, including the vacant coordination site of Cu1. The occupancy of a test oxygen atom placed coordinated to Cu1 was refined to zero. Residual nuclear density remained inside the cages including at a position consistent with solvent coordination at Cu2, indicating that this region of the structure was not available for gas binding. The positions and occupancies of CO_2 and CD_4 guest sites and host geometry were refined, while the guest molecular geometries were rigidly constrained (linear and tetrahedral for CO_2 and CD_4, respectively). The locations of the deuterium atoms in CD_4 were not determined and are likely to be mobile; they are included in the model at idealized positions to give appropriate overall nuclear scattering power. Full descriptions of the refined structures are included in the Supporting Information.

DFT Calculations. Density functional theory (DFT) calculations were performed using the Q-Chem software package[33] at the B3LYP/6-31+G* level of theory with the D3 dispersion correction scheme proposed by Grimme.[34] For Cu atoms the modified m6-31G* basis set[35] was used and the three-body dispersion contributions were added in calculations of binding energies using the standalone DFT-D3 (V3.2) code.[34] All presented values of the binding energies have been counterpoise-corrected for the basis set superposition error (BSSE).[36] Further details of DFT calculations are provided in the Supporting Information.
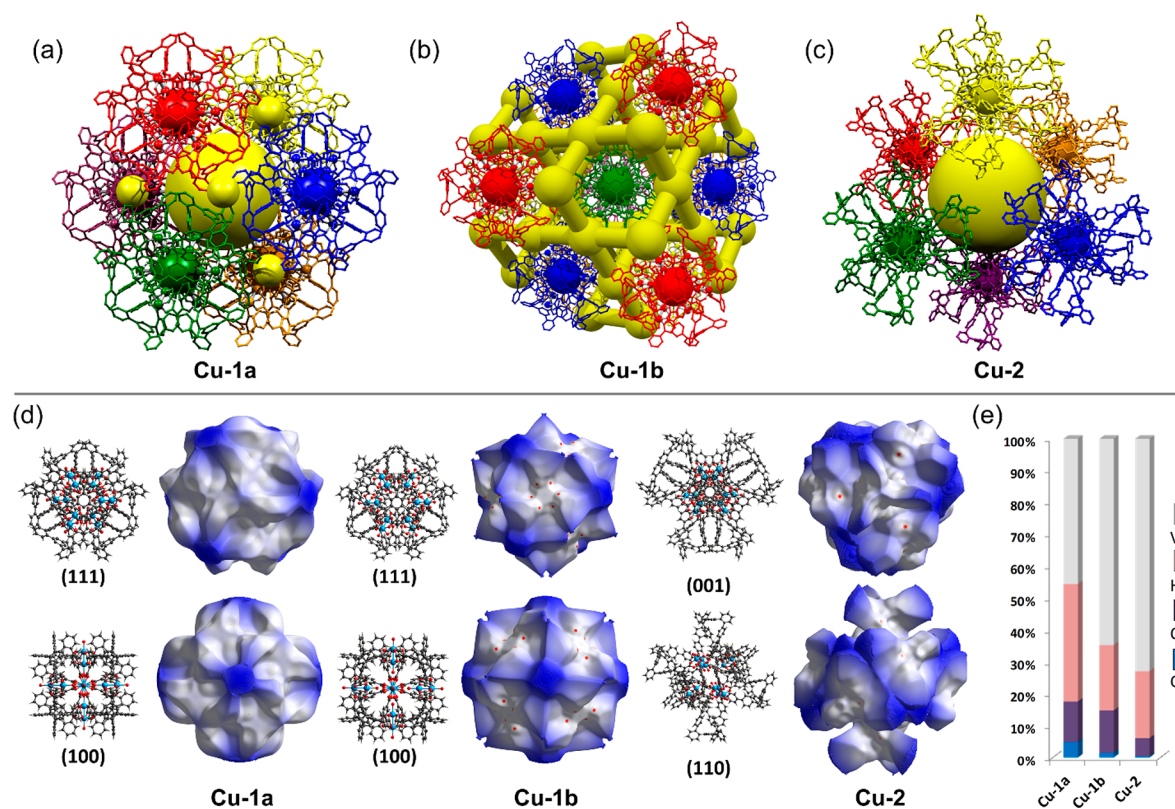
Figure 2. Views of the crystal packing of molecular cages and resultant void spaces in (a) **Cu-1a**, (b) **Cu-1b**, and (c) **Cu-2**. Color code: cages, red, green, blue, yellow, orange, maroon; internal cage cavities colored to match cages; intermolecular voids and channels, yellow. (d) Hirshfeld surfaces of the three cages viewed toward triangular faces (top), along the Cu−Cu axis of paddlewheels (bottom, **Cu-1a** and **Cu-1b**) and along the crystallographic a axis (bottom, **Cu-2**) with viewing directions given as Miller indices. The surfaces are colored to show the property d_{norm}: the normalized contact distance between the Hirshfeld surface of the molecule and the nearest nucleus outside the surface. Contacts around the sum of the van der Waals radii of the nuclei are shown in white while shorter and longer contacts are shown in red and blue, respectively. (e) Histograms showing the distributions of contact types between the cage molecules and surrounding space.

■ RESULTS AND DISCUSSION

Synthesis and Analysis of Crystal Structures. A solvothermal reaction of H_3L^1 and $Cu(NO_3)_2 \cdot 3H_2O$ in DMF at 80 °C results in the formation of the porous MOP complex **Cu-1a** with the formula $[Cu_{12}(L^1)_8(H_2O)_9 \supset (H_2O)_2] \cdot H_2O \cdot 14(DMF)$ (Figure 1a). The structure of **Cu-1a·solv** was determined by single-crystal X-ray diffraction (SCXRD), while the composition and thermal stability of the bulk material were confirmed by powder X-ray diffraction (PXRD), elemental analysis, and thermal gravimetric analysis (TGA) (Figure 1c and Figures S1 and S9). **Cu-1a** crystallizes in cubic space group $F432$ with unit cell length $a = 33.21$ Å. In the structure of **Cu-1a** eight tripodally disposed ligands $(L^1)^{3-}$ cap the triangular faces of an octahedral array of six paddlewheels. Each ligand $(L^1)^{3-}$ binds three carboxylate groups to three different paddlewheel units to give a rhombic-dodecahedral topology,[11a,37] which mutually satisfies the eight tripodal ligands and six $\{Cu\}_2$ paddlewheels (Figure 1b). The polyhedron encloses an irregular cavity with a potential volume of 272 Å^3 occupied by a mixture of disordered solvent molecules bound at inwardly pointing axial sites of the surrounding paddlewheels. Each tripodal ligand $(L^1)^{3-}$ adopts a propeller-like twisted conformation, with all eight ligands being twisted in the same sense, resulting in the cage possessing chiral octahedral O_h symmetry, leading to the crystallization of **Cu-1a** in the chiral space group as a racemic twin: clusters of both handedness are present in the crystal but are not packed

together in the same domain.[38] In **Cu-1a** the cages pack in a pseudo face-centered-cubic (fcc) arrangement, resulting in two types of intermolecular voids in the lattice: large octahedral cavities with a volume of 3336 Å^3 and small tetrahedral cavities with a volume of 114 Å^3 (Figure 2a). The two types of intermolecular voids in combination with the internal cage cavities result in the desolvated structure having a total potential void fraction of 39%, as calculated by PLATON.[30]

Interestingly, the same solvothermal reaction as above but at a lower temperature of 4 °C results in the formation of the lower density polymorph **Cu-1b**, composed of rhombic dodecahedral cages isostructural with those in **Cu-1a** (Figure 1a). The single crystal X-ray diffraction (SCXRD) structure shows that **Cu-1b** has the formula $[Cu_{12}(L^1)_8(H_2O)_{12} \supset (H_2O)_5] \cdot 12H_2O \cdot 18(DMF)$ and crystallizes in cubic space group $Pn\bar{3}n$ with the unit cell length $a = 28.75$ Å. **Cu-1b** has a significantly lower density packing arrangement compared to **Cu-1a**, resulting in a potential void fraction of 50%. The pseudo body-centered-cubic (bcc) packing of cages in **Cu-1b** results in continuous channels in the structure rather than discrete intermolecular voids in **Cu-1a**; these channels account for 45% of the porous voids with the remaining 5% found inside the cages (Figure 2b). The cages in **Cu-1b** have a larger potential internal volume (592 Å^3) in comparison to those in **Cu-1a** (272 Å^3) as a result of a flatter conformation of the tripodal ligand $(L^1)^{3-}$, which pushes the carboxylate binding moieties further apart.[15b] The

individual cages in **Cu-1b** possess the same chiral octahedral O_h symmetry observed in **Cu-1a**, but cages of both handedness are found in the centrosymmetric space group. Samples of **Cu-1b** isolated after short reaction durations of up to 48 h were found by PXRD to be phase-pure (Figure 1c), while those isolated after longer durations in solution showed increasingly broad diffraction peaks before transforming into a poorly crystalline phase of **Cu-1a**. Therefore, it is concluded that the more porous phase **Cu-1b** is a kinetic product with respect to the more thermodynamically stable but denser phase **Cu-1a**.

An attempt was made to increase the size of the MOP cages, and thus the porosity of the resultant material, by reacting the extended ligand **H3L2** with $Cu(NO_3)_2\cdot3H_2O$ in DMF, resulting in formation of large platelike crystals (Figure 1a). The complex **Cu-2** was shown by SCXRD to have the formula $[Cu_{12}(\mathbf{L^2})_8(H_2O)_{12}\supset(H_2O)_5]\cdot60(DMF)$ consisting of isotopological rhombic dodecahedral cages in comparison to those described in **Cu-1a** and **Cu-1b**. Despite elongation of the ligand arms in **H3L2** with a phenyl spacer ligand, the cages in **Cu-2** possess an octahedral arrangement of six paddlewheels similar to those found in **Cu-1a** and **Cu-1b**; the longer ligand fulfils the geometric requirements of the topology through adjustments in torsion angles between phenyl rings.[15b] In the structure of **Cu-2** the homochiral cages crystallize in trigonal space group *R*32 and pack in a pseudo fcc arrangement with very large potential void regions totaling 58% inside and between them. The void fraction outside the cages totals 56% with 2% inside the cages; thus, the major portion of permanent porosity resides between polyhedra rather than within. Inside the cage are six full-occupancy Cu(II)-bound H_2O ligands and eight half-occupancy free H_2O residues, each nestled in the 3-fold symmetric cleft of a ligand. The contents of the external void were diffuse and could not be determined (Figure 2c). The PXRD pattern of **Cu-2** after solvent exchange shows some differences from the pattern derived for the solvated form, indicating some rearrangement of packing in the structure upon loss of solvent from void spaces (Figure 1c).

Permanent Porosity and Structural Stability. The permanent porosity of the three MOP materials was confirmed by N_2 adsorption isotherms at 77 K. The N_2 isotherm for **Cu-1a** after solvent and supercritical CO_2 exchange followed by activation at 150 °C shows reversible type I behavior with type IVb characteristics and a pore volume of 0.381 cm/g, showing good agreement with that obtained from the crystal structure (0.378 cm/g) (Figure 3a, Figures S2 and S3, and Table 1). The N_2 isotherm for **Cu-1b** after it was rinsed with acetone and activated at 120 °C shows reversible type I behavior with type IVb characteristics and a degree of hysteresis beyond ca. p/p_0 0.4. The porosity of 0.495 cm/g is slightly lower than the crystallographically indicated value (0.588 cm/g). The BET surface areas for **Cu-1a** and **Cu-1b** of 751 and 885 m²/g, respectively, are high for MOPs,[7b,g,h,8,39] particularly Cu-based ones,[39b,c] though a surface area nearly twice as large has been reported recently.[18d] The N_2 isotherm for **Cu-2** after solvent exchange with acetone and activation at 120 °C shows type I behavior with type IVb characteristics; hysteresis on the return isotherm remains open to p/p_0 0.1. The pore volume is 0.289 cm/g, and a lower BET surface area of 508 m²/g is observed. The measured porosity of **Cu-2** is unsurprisingly lower than the crystallographically indicated value (0.578 cm/g) because of the observed structural collapse. The structural integrity of **Cu-1a** and **Cu-1b** and the collapse of **Cu-2** is also reflected in pore size distributions calculated from the N_2 adsorption using
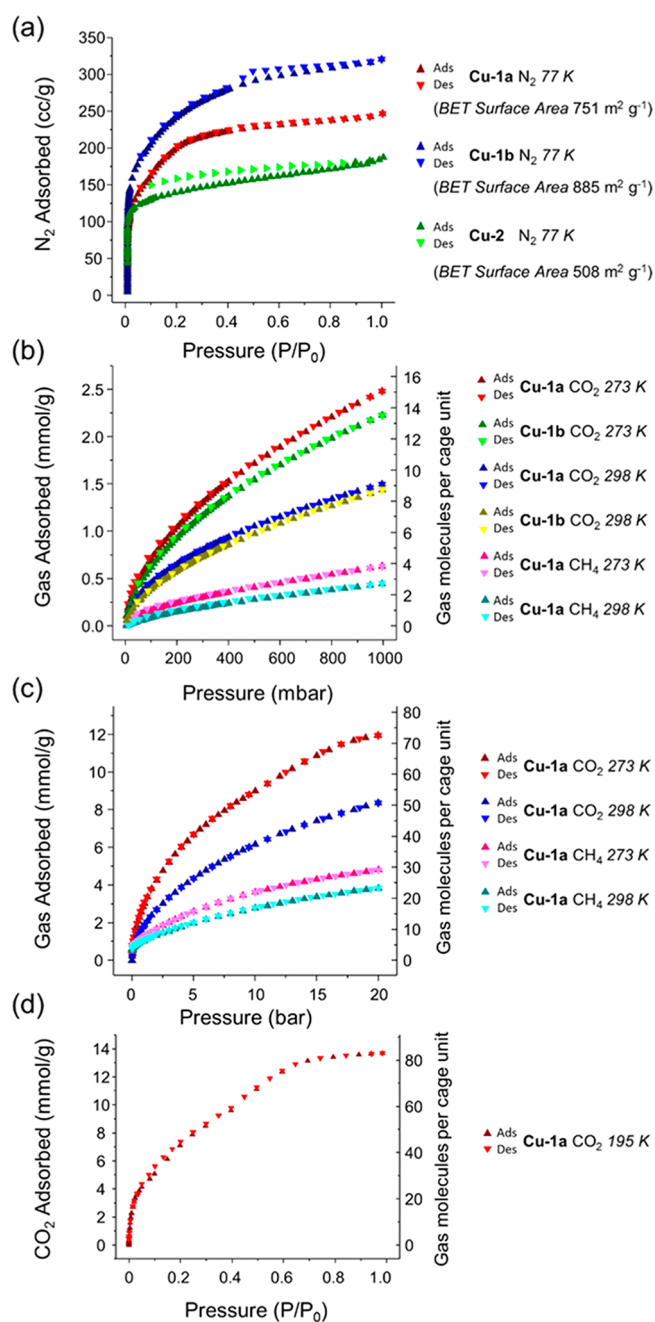

Figure 3. (a) N_2 isotherms (77 K) and calculated BET surface areas for **Cu-1a**, **Cu-1b**, and **Cu-2**. (b) Low-pressure CO_2 isotherms for **Cu-1a** and **Cu-1b** at 273 and 298 K and low-pressure CH_4 isotherms for **Cu-1a** measured at 273 and 298 K. (c) High-pressure CO_2 and CH_4 isotherms for **Cu-1a** and **Cu-1b** measured at 273 and 298 K. (d) Low-pressure CO_2 isotherm for **Cu-1a** measured at 195 K.

nonlocal density functional theory (NLDFT) methods (Figure S3b). The pore distributions for all three materials exhibit a combination of micro- and mesopores in agreement with their crystal structures, accounting for the mixture of type I and type IVb characteristics observed in their N_2 isotherms.

Hirshfeld surfaces calculated for the MOPs with non-coordinated solvents omitted illustrate subtle differences in packing interactions among the phases, allowing rationalization of the consequent differences in their stabilities with respect to their porosities: **Cu-1a** > **Cu-1b** > **Cu-2** (Figure 2d). The surfaces are colored to represent the value d_{norm}, which

Table 1. Surface Areas, Porosities, and Densities of MOP Materials[a]

	Cu-1a	Cu-1b	Cu-2
BET surface area (m^2/g)	751 ± 3.2	885 ± 2.8	508 ± 0.8
measd N_2 capacity (cm^3/g)	246.2	319.9	187.0
measd N_2 pore volume (cm^3/g)	0.381	0.495	0.289
crystallographic pore volume (cm^3/g)	0.378	0.588	0.578
crystallographic pore fraction	0.386	0.499	0.578
desolvated density (g/cm^3)	1.022	0.849	0.692

[a]The BET surface areas and measured pore volumes are determined from N_2 adsorption isotherms measured at 77 K. Crystallographic properties are calculated by PLATON with a 1.2 Å probe from SCXRD structures with all solvent molecules omitted.

describes the distance between the Hirshfeld surface of the promolecule and the closest nuclei outside the surface (Figure 2d).[40] Cages in **Cu-1a** contact 12 neighbors; no short intermolecular interactions are present, exemplified by uniform white regions on the Hirshfeld surface. In contrast, cages in **Cu-1b** contact only eight neighbors; each contact encompasses a smaller area with less uniform character, exemplified by the white regions punctuated by six small red spots on the Hirshfeld surface. The red spots represent short intermolecular contacts arising from C−H···π edge-to-face interactions (H26···Ph{C21−C26} mean-plane distance 2.77(1) Å, H26···Ph{C21−C26} centroid distance 3.00(1) Å) between neighboring cages. The Hirshfeld surface of the cage in **Cu-2** has an irregular shape featuring both small red spots and large regions of blue coloration denoting regions where the surface adjoins voids containing diffuse solvent molecules. The trend from stable packing mediated by large regions of uniform weak interactions (**Cu-1a**) toward unstable packing mediated by an irregular distribution of strong interactions, alongside large regions interfacing with voids (**Cu-2**), can also been seen in the histograms of interaction types determined during the Hirshfeld analysis (Figure 2e).

Gas Adsorption Properties. **Cu-1a** shows reversible CO_2 uptake with capacities at 1 bar of 2.48 mmol/g (273 K) and 1.50 mmol/g (298 K). High-pressure capacities of CO_2 in **Cu-1a** at 20 bar are 11.97 mmol/g (273 K) and 8.37 mmol/g (298 K). The CO_2 isotherms of **Cu-1a** at 273 K do not saturate at 20 bar; a low-temperature isotherm was measured at 195 K, indicating a saturated loading at 1 bar of 13.69 mmol/g (Figure 3d). The low-temperature CO_2 isotherm has inflections at p/p_0 values of 0.03 and 0.70 indicative of sequential pore-filling effects. The density of adsorbed CO_2 in **Cu-1a** at 195 K and 1 bar, calculated from the measured material porosity and crystallographic bulk density, was found to be 1.58 g/cm^3. This adsorbed density is among the highest reported values in porous materials[41] and is comparable with the density of dry ice (1.562 g/cm^3 at 195 K). At 20 bar, **Cu-1a** has CH_4 capacities of 4.81 mmol/g (273 K) and 3.84 mmol/g (298 K). Isosteric heats of adsorption (Q_{st}) for CO_2 and CH_4 in **Cu-1a** calculated using the virial method are 21.0 and 28.6 kJ/mol, respectively (Figure S6). The larger Q_{st} value for CH_4 over that for CO_2 in **Cu-1a** is an unusual observation, indicating the presence of strong binding sites specific to CH_4 in **Cu-1a**. We believe that the high affinity of methane for the small tetrahedral cavities in **Cu-1a** is responsible for the stronger binding; this hypothesis is supported by our subsequent neutron powder diffraction (NPD) and DFT studies.

Interestingly, **Cu-1a** was shown to retain its CO_2 adsorption capacity after a cycle of activation, rehydration (*via* dosing with hot water vapor), and reactivation (Figure S5). This type of behavior, recently reported in a Zr-based MOP,[42] contrasts with that of many MOFs containing {Cu}$_2$ paddlewheels, which lose structural integrity (and hence porosity) upon rehydration of activated samples.[43] The resilience of **Cu-1a** to rehydration is likely attributed to the nature of MOP-based porous materials; thus, no covalent bond is required to support the 3D framework and a change in the local coordination environment of {Cu}$_2$ paddlewheels has a minimal effect on the global structure.

***In Situ* IR Spectroscopy.** To probe the interaction between **Cu-1a** and CO_2 further, *in situ* IR spectroscopy was used to monitor changes in the combination band region (3500−3800 cm^{-1}). This region was chosen because the fundamental antisymmetric band at 2348 cm^{-1} has an absorbance considerably greater than 1 at pressures above 0.2 bar, whereas the bands in this region are significantly less intense. When a KBr disk, in the absence of **Cu-1a**, was exposed to 0−1 bar of CO_2 at 195 K, two gas-phase IR combination bands are observed, centered at 3714 and 3612 cm^{-1}, which are assigned to the $2\nu_2 + \nu_3$ and $\nu_1 + \nu_3$ bands, respectively (Figure 4a).[44] When a solvent-exchanged and degassed sample of **Cu-1a** pressed in a KBr pellet was exposed to various pressures of CO_2 at temperatures of 195 and 273 K, two bands were observed to grow at 3690 and 3583 cm^{-1} with increasing pressure of CO_2. These bands are consistent with
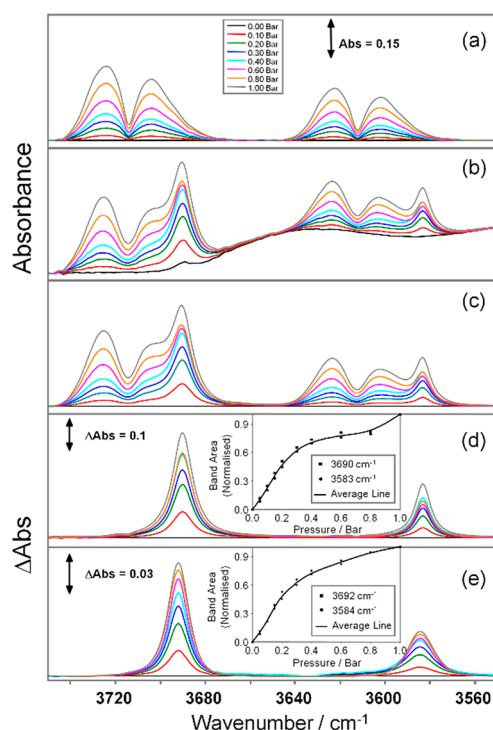

Figure 4. *In situ* FTIR spectra of CO_2 at various pressures (0−1 bar) in the combination region at 195 K (a−d) and 273 K (e): (a) spectrum of KBr + CO_2; (b) spectrum of KBr + CO_2 + **Cu-1a**; (c) spectrum (b) with the spectrum of the MOP background subtracted from it; (d) spectrum (c) minus spectrum (a) at 195 K; (e) spectrum (d) at 273 K. Insets: plots showing the normalized band areas of the two peaks assigned to adsorbed CO_2 in **Cu-1a** as a function of pressure.
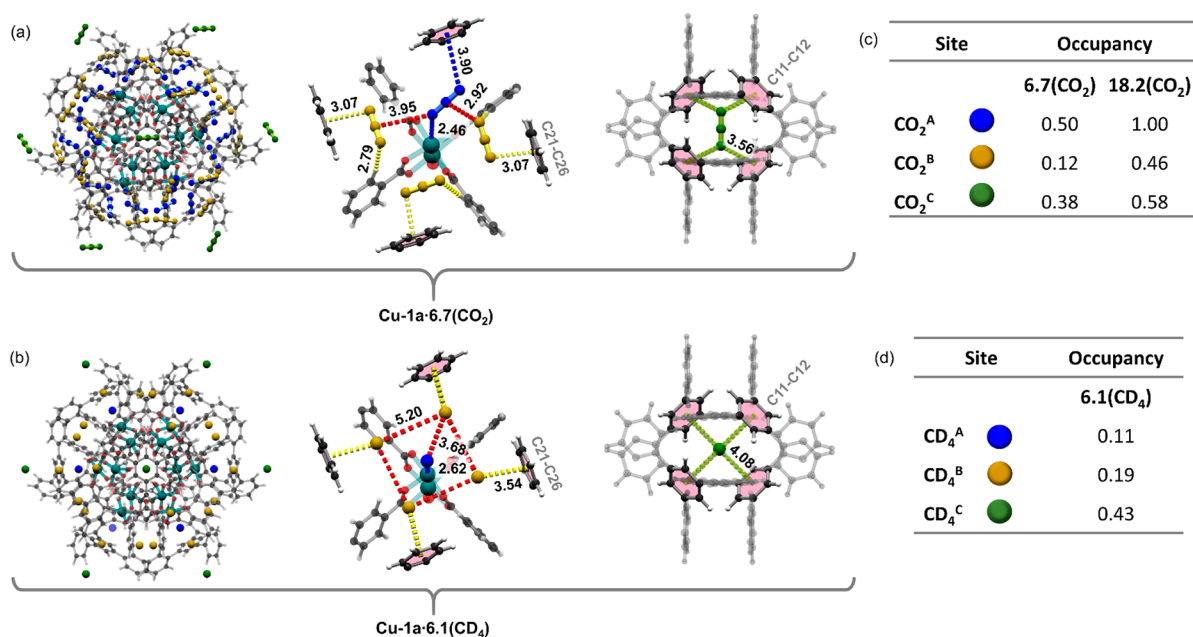
Figure 5. Binding sites of (a) CO_2^{A-C} and (b) CD_4^{A-C} in **Cu-1a·6.7CO₂** and **Cu-1a·6.1CD₄** determined by Rietveld refinement of NPD data collected at 10 K. Refined chemical site occupancies and color coding of guest sites for (c) CO_2^{A-C} and (d) CD_4^{A-C}. Selected intermolecular distances are labeled in Å. Color code: carbon, black; oxygen, red; hydrogen, white; copper, teal; guest molecules, blue, yellow, and green.

adsorption of CO_2 within the pores of **Cu-1a**.[45] The IR spectrum of **Cu-1a** contains a broad band in this region, which does not appear to change significantly with increasing pressure. Therefore, the spectrum recorded at 0 bar of CO_2 was used as a background spectrum (Figure 4c). After background subtraction, spectra were obtained free of contributions from the host material and gas-phase CO_2 (Figure 4d) and these showed two peaks assigned to the adsorbed CO_2 phase. The band areas of the adsorbed phase were obtained (Figure 4d, inset), showing the change in CO_2 uptake with pressure. These data were normalized such that the band areas at 1 bar have been set to 1; the same procedure was performed at 273 K, and the spectra obtained after subtraction of the gas phase are shown in Figure 4e. Two bands for adsorbed CO_2 are observed at 3692 and 3584 cm⁻¹, and the change in band area as the pressure is varied is shown in the inset figures (Figure 4). These plots show qualitative agreement with volumetrically and gravimetrically measured CO_2 isotherms for **Cu-1a** at 195 and 273 K. The IR bands of **Cu-1a** show minimal change with increasing pressure of CO_2 at both temperatures, consistent with previous reports of CO_2 uptake in MOFs.[17]

Determination of Binding Sites for Adsorbed CO_2 and CH_4 Molecules in Cu-1a. Both *in situ* NPD and SCXRD experiments were used to probe the adsorption sites of CO_2 and CD_4 in desolvated **Cu-1a**. While NPD experiments demonstrate contrasting binding site preferences for the two gases, the SCXRD experiment using a partially hydrated crystal confirms an important interaction between CO_2 and a copper-bound water molecule.

Rietveld refinements of data measured at 10 K with loadings of 6 CO_2, 18 CO_2, and 6 CD_4 molecules per Cu_{12} cage revealed three binding sites common to both CO_2 and CD_4 guests in the resultant structures **Cu-1a·6.7CO₂**, **Cu-1a·18.6CO₂**, and **Cu-1a·6.1CD₄** (Figure 5). Site occupancies for guests CO_2^{A-C} and CD_4^{A-C} were refined with globally fixed atomic displacement parameters. Contrasting binding prefer-

ences are evident for CO_2 and CD_4: the most populated site in **Cu-1a·6.7CO₂** is CO_2^A adjacent to external Cu(II) sites, whereas the most populous site in **Cu-1a·6.1CD₄** is CD_4^C located in the small tetrahedral void. This observation agrees with the expectation that CO_2 can act as a weak Lewis base, allowing it to coordinate to the open Cu(II) site (O1A···Cu(1) = 2.46(5) Å). Site CO_2^B in **Cu-1a·6.7CO₂** is adjacent to a phenyl ring (O1B···Ph{C21−C26} centroid = 3.07(5) Å) and has the lowest occupancy of the three sites. Site CO_2^B also accepts a weak supramolecular bond from a phenyl C−H donor (C35−H35···O3B$_{CO2}$ = 2.79(3) Å; angle 166(1)°).[16b,46] Potential favorable intermolecular $C^{\delta+}···O^{\delta-}$ contacts exist between sites CO_2^A and CO_2^B (C2A···O3B and C2B···O1A = 2.92(8) and 3.95(6) Å, respectively). Site CO_2^C, located in the small tetrahedral void in **Cu-1a·6.7CO₂**, has a high occupancy comparable to that of CO_2^A on Cu(II) sites; it makes four equal interactions with the surrounding phenyl rings (O1C···Ph{C11−C12} centroid = 3.56(1) Å). CD_4 cannot form strong coordinate bonds, and thus in **Cu-1a·6.1CD₄** CD_4^A adjacent to Cu(II) (Cu1···C1A = 2.62(5) Å) has the lowest occupancy of the three CD_4 sites. CD_4^B adjacent to a single phenyl ring has an intermediate occupancy, while CD_4^C in the small tetrahedral void has the highest occupancy. CD_4^B makes a close contact with a single phenyl ring (C1B···Ph{C21−C26} centroid = 3.54(1) Å), while CD_4^C makes four equal longer contacts with the surrounding phenyl rings (C1C···Ph{C11−C12} centroid = 4.08(1) Å). Adjacent sites CD_4^A and CD_4^B in **Cu-1a·6.1CD₄** have a C···C distance of 3.68(1) Å, significantly shorter than the C···C distance of 4.08 Å in the α polymorph of CD_4 at 1.5−6 K.[47] The plausibility of these adjacent sites being simultaneously occupied is confirmed by DFT calculations (see below). Upon an increase in the loading of CO_2 in **Cu-1a·18.6CO₂** the refined occupancies of CO_2^{A-C} increase while their positions show only minor changes (Figure S20). Site CO_2^A coordinated to Cu(II) remains the most populated, reaching saturation, while the occupancies of CO_2^B and CO_2^C increase to similar values of 0.46(1) and 0.58(1),

respectively. Thus, this study has afforded a sharp comparison of the MOP−gas binding between CO_2 and CD_4 at atomic resolution and represents the first example of such in an unpillared MOP material.[18d]

We also sought to understand the effect of Cu(II)-bound water on CO_2 binding from a structural perspective. An inspection of electron density maps and analysis using PLATON SQUEEZE for **Cu-1a·H_2O** showed complete removal of free solvent from the large octahedral void and small tetrahedral void along with retention of coordinated water on both Cu(II) paddlewheel axial sites (Tables S4 and S5). The retention of coordinated water despite prolonged heating under vacuum reflects the difficulty of activating a large monolithic single crystal in contrast to microcrystalline powder samples used in NPD experiments. The presence of the Cu(II)-bound water in the structure **Cu-1a·H_2O** afforded a unique opportunity to examine the binding of CO_2 in the hydrated material: data were collected for the gas-loaded structure **Cu-1a·H_2O−CO_2** at 120 K. Guest binding sites were found adjacent to the coordinated water in the large octahedral void (Figure 6) and at the center of the small tetrahedral void.
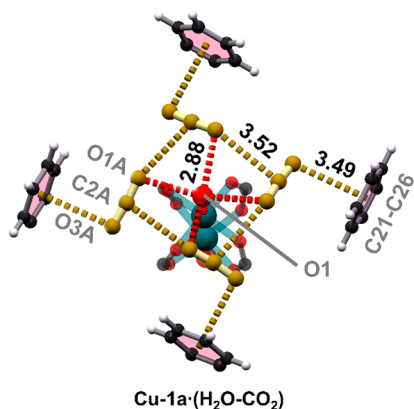

Cu-1a·(H_2O-CO_2)

Figure 6. View of CO_2 binding environments at the copper paddlewheel in **Cu-1a·H_2O−CO_2** determined by *in situ* SCXRD at 120 K. Selected intermolecular distances are labeled in Å. Color code: carbon, black; oxygen, red; hydrogen, white; copper, teal; guest CO_2, yellow.

The CO_2 site in the large octahedral void is in a location similar to that of CO_2^B found by NPD; however, it simultaneously takes part in three types of interactions: accepting a hydrogen bond from the coordinated water molecule ($O1_{H2O}···O1A_{CO2} = 2.88(6)$ Å), interacting with the adjacent phenyl ring ($O3A_{CO2}···Ph\{C21−C26\}$ centroid = 3.49(6) Å), and making favorable $C^{\delta+}···O^{\delta-}$ contacts with symmetry-equivalent neighbors ($C2A_{CO2}···O1A_{CO2} = 3.52(7)$ Å). The hydrogen atoms on the coordinated water molecule were not observed in the electron density map; the presence of a hydrogen bond is deduced from atomic positions and supported by DFT calculations (*vide infra*). This structure represents the first crystallographic evidence of the mechanism by which partial hydration of Cu(II)-containing MOFs may lead to enhanced CO_2 adsorption properties.

DFT Calculations and Analysis of the Host−Guest Binding Energies. DFT calculations have been used to probe further the CO_2 and CH_4 binding sites in **Cu-1a**. Host fragments representing one edge of the large octahedral void and the small tetrahedral void in **Cu-1a** were used to simulate environments analogous to sites $CO_2^{A−C}$ and $CD_4^{A−C}$

determined by NPD. Structures obtained by NPD were chosen as starting configurations, and positions of guest molecules were fully optimized. The calculated minimum energy configurations were found to be in a good agreement with the experimentally determined structures. Binding energies were then calculated for the guests in the optimized geometries. The results of DFT calculations are summarized in Table 2.

At the equivalent adsorption sites, binding energies of CO_2 molecules were found to be higher than those of CH_4 molecules. The values of −27.9 and −28.0 kJ/mol were predicted for the sites CO_2^{Cu} and CO_2^{Ph}, analogous to NPD sites CO_2^A and CO_2^B, while for the sites CH_4^{Cu} and CH_4^{Ph}, analogous to CD_4^A and CD_4^B, the binding energies were calculated to be −22.9 and −20.5 kJ/mol, respectively. For both guest molecules, the most energetically favorable adsorption configurations were found to be inside the small tetrahedral void with binding energies of −39.5 and −31.5 kJ/mol for CO_2^{Tet*} and CH_4^{Tet}, respectively. It should be noted that experimentally determined sites CO_2^C and CD_4^C are centered on the crystallographic special positions in the middle of the void. The special position is at (0.25, 0.25, 0.25) and lies at the intersection of three four-fold screw axes and four three-fold proper rotation axes. However, in the case of a CO_2 guest molecule the DFT calculations predict the lowest energy CO_2^{Tet*} position to be shifted by 0.92 Å toward the void edge. The binding energy for the site CO_2^{Tet} in the middle of the void was calculated to be −32.9 kJ/mol, which is significantly smaller than the value found for the CO_2^{Tet*} site.

Further calculations were performed to investigate interactions between guest molecules at close-lying binding sites determined from the diffraction experiments. In this context, the diffraction experiments are ambiguous, since it is uncertain whether adjacent partially occupied crystallographic sites are populated simultaneously. Three configurations of CO_2^{Cu}−CO_2^{Ph} molecular pairs were considered on the basis of the NPD structures (see Table 2). Binding energies of $CO_2^{Ph\ddagger1−3}$ were calculated to be −32.0, −33.3, and −29.1 kJ/mol, respectively. The two most strongly bound conformations, $CO_2^{Ph\ddagger1}$ and $CO_2^{Ph\ddagger2}$, both feature slipped parallel arrangements with the adjacent $CO_2^{Cu\ddagger}$ guest, resulting in pairs of electrostatically favorable intermolecular contacts (the $C^{\delta+}···O^{\delta-}$ distance ranges between 3.22−3.66 Å). The more weakly bound site $CO_2^{Ph\ddagger3}$ interacts with $CO_2^{Cu\ddagger3}$ in a T-type conformation making a single, longer intermolecular contact ($C^{\delta+}···O^{\delta-} = 3.67$ Å). The above results show that interactions between CO_2 guest molecules can increase the binding energy by 4−5 kJ/mol. This suggests that CO_2 guests, observed with partial occupancies in the diffraction experiments, are likely to occupy adjacent binding sites in the same voids. No comparable energy gain is observed for a pair of neighboring CH_4 guests: the calculated binding energy of −21.6 kJ/mol for $CH_4^{Ph\ddagger}$ is only 1 kJ/mol larger than that for the single-occupancy site CH_4^{Ph}.

Similar calculations were performed for a CO_2 guest adjacent to the Cu(II)-bound water molecule in a hydrated fragment, analogous to that observed by SCXRD in **Cu-1a·H_2O−CO_2**.[25a] The binding energy of $CO_2^{Ph§}$ was calculated to be −41.0 kJ/mol, which is significantly higher than for a single CO_2^{Ph} guest. The calculations confirm that $CO_2^{Ph§}$ is in a suitable position to accept a strong hydrogen bond from the coordinated water with $O_{H2O}···O_{CO2} = 2.96$ Å, and $<O−H···O_{CO2} = 150.7°$.

Table 2. DFT Optimized Guest Geometries and Calculated Binding Energies for CO_2 and CH_4 in Local Fragments of Cu-1a

Single guest geometry optimizations[a]			Pairwise guest geometry optimizations[b]		
Full Fragment	Local Environment	Binding Energy[c] (kJ/mol)	Full Fragment	Local Environment	Binding Energy[d] (kJ/mol)
	3.97 ... 2.46	-27.9 ($CO_2{}^{Cu}$) -22.9 ($CH_4{}^{Cu}$)		3.59, 3.22, 3.38	-32.0 ($CO_2{}^{Ph\ddagger1}$) -21.6 ($CH_4{}^{Ph\ddagger1}$)
DFT: $CO_2{}^{Cu}$ (*pink*); **NPD**: $CO_2{}^{A}$ (*blue*)			**DFT**: $CO_2{}^{Cu\ddagger1}$ (*blue*) and $CO_2{}^{Ph\ddagger1}$ (*pink*)		
	3.26	-28.0 ($CO_2{}^{Ph}$) -20.5 ($CH_4{}^{Ph}$)		3.35, 3.29, 3.66	-33.3 ($CO_2{}^{Ph\ddagger2}$)
DFT: $CO_2{}^{Ph}$ (*pink*); **NPD**: $CO_2{}^{B}$ (*yellow*)			**DFT**: $CO_2{}^{Cu\ddagger2}$ (*blue*) and $CO_2{}^{Ph\ddagger2}$ (*pink*)		
	3.73 ... 3.56	-32.9 ($CO_2{}^{C}$) -39.5 ($CO_2{}^{Tet*}$)		3.28, 3.67	-29.1 ($CO_2{}^{Ph\ddagger3}$)
DFT: $CO_2{}^{Tet*}$ (*pink*); **NPD**: $CO_2{}^{C}$ (*green*)			**DFT**: $CO_2{}^{Cu\ddagger3}$ (*blue*) and $CO_2{}^{Ph\ddagger3}$ (*pink*)		
	4.08	-31.5 ($CD_4{}^{Tet}$)		3.67, 2.07	-41.0 ($CO_2{}^{Ph\S}$)
DFT: $CH_4{}^{Tet}$ (*pink*)			**DFT**: H_2O^{Cu} (*red*) and $CO_2{}^{Ph\S}$ (*pink*)		

■ CONCLUSIONS

We report a detailed investigation into the permanent porosities and gas adsorption properties of a family of three MOPs constructed from {Cu}₂ paddlewheels and tripodally disposed tris-carboxylate ligands. The formation of stable, permanently porous molecular solids from MOPs is rare, as the materials are prone to structural collapse upon removal of reaction solvent from their void spaces. The order of decreasing structural resilience to solvent removal for the MOPs (**Cu-1a** > **Cu-1b** > **Cu-2**) has been rationalized by using Hirshfeld surfaces to analyze the supramolecular interactions which mediate their molecular packing. The most stable material, **Cu-1a**, has the highest density of the

three, and its molecular packing is exclusively mediated by large regions of weak van der Waals interactions with a notable absence of any stronger π−π or edge-to-face stacking interactions. The high uptake of CO_2 and CH_4 in permanently porous **Cu-1a** has been probed using a combination of IR spectroscopy, *in situ* neutron and X-ray diffraction, and DFT modeling of the experimentally elucidated host−guest binding interactions. The different types of voids in **Cu-1a** present a platform for comparing the contrasting binding preferences of these industrially and environmentally important gases. CO_2 shows a roughly equal propensity to bind at either an open metal site or a small tetrahedral void enclosed by phenyl rings, while CD_4 shows a preference for the latter site. It is interesting

to note that packing coefficients of 0.33 and 0.28, respectively, for CO_2 and CH_4 in the small tetrahedral void (molecular volumes: CO_2, 34.0 Å^3; CH_4, 28.5 Å^3; small void, 102 Å^3)[48] are the closest matches in the structure to the optimum packing coefficient of 0.55 ± 0.009 suggested by Mercozzi and Rebek for guest binding inside receptor cavities.[49] The use of multiple analytical techniques to probe the host–guest interactions in **Cu-1a** gives a validated structural insight into design features used commonly used to target CO_2 and CH_4 adsorption in porous MOP materials.

■ ASSOCIATED CONTENT

Ⓢ Supporting Information

The Supporting Information is available free of charge at https://pubs.acs.org/doi/10.1021/acs.inorgchem.0c01935.

> Experimental details for single-crystal structure refinements, powder diffraction data, DFT calculations, and supporting figures and tables (PDF)

Accession Codes

CCDC 1516122−1516130 contain the supplementary crystallographic data for this paper. These data can be obtained free of charge via www.ccdc.cam.ac.uk/data_request/cif, or by emailing data_request@ccdc.cam.ac.uk, or by contacting The Cambridge Crystallographic Data Centre, 12 Union Road, Cambridge CB2 1EZ, UK; fax: +44 1223 336033.

■ AUTHOR INFORMATION

Corresponding Authors

Stephen P. Argent − *School of Chemistry, University of Nottingham, Nottingham NG7 2RD, U.K.;* Email: stephen.argent@nottingham.ac.uk

Neil R. Champness − *School of Chemistry, University of Nottingham, Nottingham NG7 2RD, U.K.;* ⓘ orcid.org/0000-0003-2970-1487; Email: neil.champness@nottingham.ac.uk

Martin Schröder − *School of Chemistry, University of Nottingham, Nottingham NG7 2RD, U.K.; Department of Chemistry, University of Manchester, Manchester M13 9PL, U.K.;* ⓘ orcid.org/0000-0001-6992-0700; Email: M.Schroder@manchester.ac.uk

Authors

Ivan da Silva − *ISIS Facility, STFC Rutherford Appleton Laboratory, Chilton, Oxfordshire OX11 0QX, U.K.*

Alex Greenaway − *School of Chemistry, University of Nottingham, Nottingham NG7 2RD, U.K.; R92 Research Complex at Harwell, Rutherford Appleton Laboratory, Didcot, Oxfordshire OX11 0DE, U.K.*

Mathew Savage − *Department of Chemistry, University of Manchester, Manchester M13 9PL, U.K.*

Jack Humby − *Department of Chemistry, University of Manchester, Manchester M13 9PL, U.K.*

Andrew J. Davies − *School of Chemistry, University of Nottingham, Nottingham NG7 2RD, U.K.*

Harriott Nowell − *Diamond Light Source, Didcot, Oxfordshire OX11 0DE, U.K.*

William Lewis − *School of Chemistry, University of Nottingham, Nottingham NG7 2RD, U.K.;* ⓘ orcid.org/0000-0001-7103-6981

Pascal Manuel − *ISIS Facility, STFC Rutherford Appleton Laboratory, Chilton, Oxfordshire OX11 0QX, U.K.*

Chiu C. Tang − *Diamond Light Source, Didcot, Oxfordshire OX11 0DE, U.K.*

Alexander J. Blake − *School of Chemistry, University of Nottingham, Nottingham NG7 2RD, U.K.*

Michael W. George − *School of Chemistry, University of Nottingham, Nottingham NG7 2RD, U.K.;* ⓘ orcid.org/0000-0002-7844-1696

Alexander V. Markevich − *School of Chemistry, University of Nottingham, Nottingham NG7 2RD, U.K.; Faculty of Physics, University of Vienna, 1090 Wien, Austria*

Elena Besley − *School of Chemistry, University of Nottingham, Nottingham NG7 2RD, U.K.;* ⓘ orcid.org/0000-0002-9910-7603

Sihai Yang − *School of Chemistry, University of Nottingham, Nottingham NG7 2RD, U.K.; Department of Chemistry, University of Manchester, Manchester M13 9PL, U.K.;* ⓘ orcid.org/0000-0002-1111-9272

Complete contact information is available at:
https://pubs.acs.org/10.1021/acs.inorgchem.0c01935

Notes

The authors declare no competing financial interest.

■ ACKNOWLEDGMENTS

■ REFERENCES

(1) Zhou, H.-C. J.; Kitagawa, S. Metal-organic frameworks (MOFs). *Chem. Soc. Rev.* **2014**, *43*, 5415.

(2) Ding, S.-Y.; Wang, W. Covalent organic frameworks (COFs). From design to applications. *Chem. Soc. Rev.* **2013**, *42*, 548.

(3) Wu, D.; Xu, F.; Sun, B.; Fu, R.; He, H.; Matyjaszewski, K. Design and preparation of porous polymers. *Chem. Rev.* **2012**, *112*, 3959.

(4) (a) Yang, W.; Greenaway, A.; Lin, X.; Matsuda, R.; Blake, A. J.; Wilson, C.; Lewis, W.; Hubberstey, P.; Kitagawa, S.; Champness, N. R.; Schröder, M. Exceptional thermal stability in a supramolecular organic framework: porosity and gas storage. *J. Am. Chem. Soc.* **2010**, *132*, 14457. (b) Tian, J.; Thallapally, P. K.; McGrail, B. P. Porous organic molecular materials. *CrystEngComm* **2012**, *14*, 1909.

(5) Slater, A. G.; Cooper, A. I. Function-led design of new porous materials. *Science* **2015**, *348*, aaa8075.

(6) (a) Carrington, E. J.; Vitorica-Yrezabal, I. J.; Brammer, L. Crystallographic studies of gas sorption in metal-organic frameworks. *Acta Crystallogr., Sect. B: Struct. Sci., Cryst. Eng. Mater.* **2014**, *70*, 404. (b) Han, X.; Yang, S.; Schröder, M. Porous metal−organic frameworks as emerging sorbents for clean air. *Nat. Rev. Chem.* **2019**, *3*, 108. (c) Duong, T. D.; Sapchenko, S. A.; da Silva, I.; Godfrey, H. G. W.; Cheng, Y.; Daemen, L. L.; Manuel, P.; Frogley, M. D.; Cinque, G.; Ramirez-Cuesta, A. J.; Yang, S.; Schröder, M. Observation of binding of carbon dioxide to nitro-decorated metal−organic frameworks. *Chem. Sci.* **2020**, *11*, 5339.

(7) (a) Gosselin, E. J.; Decker, G. E.; Antonio, A. M.; Lorzing, G. R.; Yap, G. P. A.; Bloch, E. D. A charged coordination cage-based porous salt. *J. Am. Chem. Soc.* **2020**, *142*, 9594. (b) Duriska, M. B.; Neville, S. M.; Lu, J.; Iremonger, S. S.; Boas, J. F.; Kepert, C. J.; Batten, S. R. Systematic metal variation and solvent and hydrogen-gas storage in

supramolecular nanoballs. *Angew. Chem., Int. Ed.* **2009**, *48*, 8919. (c) Park, J.; Chen, Y.-P.; Perry, Z.; Li, J.-R.; Zhou, H.-C. Preparation of core−shell coordination molecular assemblies via the enrichment of structure-directing "codes" of bridging ligands and metathesis of metal units. *J. Am. Chem. Soc.* **2014**, *136*, 16895. (d) Augustyniak, A. W.; Fandzloch, M.; Domingo, M.; Lakomska, I.; Navarro, J. A. R. A vanadium(iv) pyrazolate metal-organic polyhedron with permanent porosity and adsorption selectivity. *Chem. Commun.* **2015**, *51*, 14724. (e) Sudik, A. C.; Millward, A. R.; Ockwig, N. W.; Côté, A. P.; Kim, J.; Yaghi, O. M. Design, synthesis, structure, and gas (N_2, Ar, CO_2, CH_4, and H_2) sorption properties of porous metal-organic tetrahedral and heterocuboidal polyhedra. *J. Am. Chem. Soc.* **2005**, *127*, 7110. (f) Boer, S. A.; White, K. F.; Slater, B.; Emerson, A. J.; Knowles, G. P.; Donald, W. A.; Thornton, A. W.; Ladewig, B. P.; Bell, T. D. M.; Hill, M. R.; Chaffee, A. L.; Abrahams, B. F.; Turner, D. R. A multifunctional, charge-neutral, chiral octahedral $M_{12}L_{12}$ cage. *Chem. - Eur. J.* **2019**, *25*, 8489. (g) Park, J.; Perry, Z.; Chen, Y.-P.; Bae, J.; Zhou, H.-C. Chromium(II) metal−organic polyhedra as highly porous materials. *ACS Appl. Mater. Interfaces* **2017**, *9*, 28064. (h) Rowland, C. A.; Lorzing, G. R.; Gosselin, E. J.; Trump, B. A.; Yap, G. P. A.; Brown, C. M.; Bloch, E. D. Methane storage in paddlewheel-based porous coordination cages. *J. Am. Chem. Soc.* **2018**, *140*, 11153. (i) Xing, W.-H.; Li, H.-Y.; Dong, X.-Y.; Zang, S.-Q. Robust multifunctional Zr-based metal−organic polyhedra for high proton conductivity and selective CO_2 capture. *J. Mater. Chem. A* **2018**, *6*, 7724. (j) Craig, G. A.; Larpent, P.; Kusaka, S.; Matsuda, R.; Kitagawa, S.; Furukawa, S. Switchable gate-opening effect in metal−organic polyhedra assemblies through solution processing. *Chem. Sci.* **2018**, *9*, 6463.

(8) (a) Lorzing, G. R.; Trump, B. A.; Brown, C. M.; Bloch, E. D. Selective gas adsorption in highly porous chromium(II)-based metal−organic polyhedra. *Chem. Mater.* **2017**, *29*, 8583. (b) Teo, J. M.; Coghlan, C. J.; Evans, J. D.; Tsivion, E.; Head-Gordon, M.; Sumby, C. J.; Doonan, C. J. Hetero-bimetallic metal-organic polyhedra. *Chem. Commun.* **2016**, *52*, 276.

(9) Cook, T. R.; Zheng, Y. R.; Stang, P. J. Metal-organic frameworks and self-assembled supramolecular coordination complexes: comparing and contrasting the design, synthesis, and functionality of metal-organic materials. *Chem. Rev.* **2013**, *113*, 734.

(10) Green, H. R.; Lloyd, G. O. In *Functional Supramolecular Materials: From Surfaces to MOFs*; The Royal Society of Chemistry: 2017; p 297.

(11) (a) Tranchemontagne, D. J.; Ni, Z.; O'Keeffe, M.; Yaghi, O. M. Reticular chemistry of metal-organic polyhedra. *Angew. Chem., Int. Ed.* **2008**, *47*, 5136. (b) Pasquale, S.; Sattin, S.; Escudero-Adan, E. C.; Martinez-Belmonte, M.; de Mendoza, J. Giant regular polyhedra from calixarene carboxylates and uranyl. *Nat. Commun.* **2012**, *3*, 785.

(12) (a) Bojdys, M. J.; Briggs, M. E.; Jones, J. T.; Adams, D. J.; Chong, S. Y.; Schmidtmann, M.; Cooper, A. I. Supramolecular engineering of intrinsic and extrinsic porosity in covalent organic cages. *J. Am. Chem. Soc.* **2011**, *133*, 16566. (b) Dai, F.-R.; Sambasivam, U.; Hammerstrom, A. J.; Wang, Z. Synthetic supercontainers exhibit distinct solution versus solid state guest-binding behavior. *J. Am. Chem. Soc.* **2014**, *136*, 7480.

(13) Slater, A. G.; Little, M. A.; Pulido, A.; Chong, S. Y.; Holden, D.; Chen, L.; Morgan, C.; Wu, X.; Cheng, G.; Clowes, R.; Briggs, M. E.; Hasell, T.; Jelfs, K. E.; Day, G. M.; Cooper, A. I. Reticular synthesis of porous molecular 1D nanotubes and 3D networks. *Nat. Chem.* **2017**, *9*, 17.

(14) Zhang, G.; Presly, O.; White, F.; Oppel, I. M.; Mastalerz, M. A shape-persistent quadruply interlocked giant cage catenane with two distinct pores in the solid state. *Angew. Chem., Int. Ed.* **2014**, *53*, 5126.

(15) (a) Argent, S. P.; Greenaway, A.; Gimenez-Lopez, M. d. C.; Lewis, W.; Nowell, H.; Khlobystov, A. N.; Blake, A. J.; Champness, N. R.; Schröder, M. High-nuclearity metal-organic nanospheres: a Cd_{66} ball. *J. Am. Chem. Soc.* **2012**, *134*, 55. (b) Argent, S. P.; Tarassova, I.; Greenaway, A.; Nowell, H.; Barnett, S. A.; Warren, M. R.; Tang, C. C.; Morris, C. G.; Lewis, W.; Champness, N. R.; Schröder, M.; Blake, A. J. Assembly of high nuclearity clusters from a family of tripodal tris-

carboxylate ligands. *Polyhedron* **2016**, *120*, 18. (c) Rajput, L.; Kim, D.; Lah, M. S. Conformational control of ligands to create a finite metal−organic cluster and an extended metal−organic framework. *CrystEngComm* **2013**, *15*, 259. (d) He, Y.-C.; Yang, J.; Kan, W.-Q.; Ma, J.-F. An ideal metal-organic rhombic dodecahedron for highly efficient adsorption of dyes in an aqueous solution. *CrystEngComm* **2013**, *15*, 848.

(16) (a) Baek, S. B.; Moon, D.; Graf, R.; Cho, W. J.; Park, S. W.; Yoon, T.-U.; Cho, S. J.; Hwang, I.-C.; Bae, Y.-S.; Spiess, H. W.; Lee, H. C.; Kim, K. S. High-temperature in situ crystallographic observation of reversible gas sorption in impermeable organic cages. *Proc. Natl. Acad. Sci. U. S. A.* **2015**, *112*, 14156. (b) Hu, X.-L.; Gong, Q.-H.; Zhong, R.-L.; Wang, X.-L.; Qin, C.; Wang, H.; Li, J.; Shao, K.-Z.; Su, Z.-M. Evidence of amine−CO_2 interactions in two pillared-layer MOFs probed by X-ray crystallography. *Chem. - Eur. J.* **2015**, *21*, 7238. (c) Sotelo, J.; Woodall, C. H.; Allan, D. R.; Gregoryanz, E.; Howie, R. T.; Kamenev, K. V.; Probert, M. R.; Wright, P. A.; Moggach, S. A. Locating gases in porous materials: cryogenic loading of fuel-related gases into a Sc-based metal−organic framework under extreme pressures. *Angew. Chem., Int. Ed.* **2015**, *54*, 13332. (d) Queen, W. L.; Hudson, M. R.; Bloch, E. D.; Mason, J. A.; Gonzalez, M. I.; Lee, J. S.; Gygi, D.; Howe, J. D.; Lee, K.; Darwish, T. A.; James, M.; Peterson, V. K.; Teat, S. J.; Smit, B.; Neaton, J. B.; Long, J. R.; Brown, C. M. Comprehensive study of carbon dioxide adsorption in the metal-organic frameworks M_2(dobdc) (M = Mg, Mn, Fe, Co, Ni, Cu, Zn). *Chem. Sci.* **2014**, *5*, 4569.

(17) (a) Stavitski, E.; Pidko, E. A.; Couck, S.; Remy, T.; Hensen, E. J. M.; Weckhuysen, B. M.; Denayer, J.; Gascon, J.; Kapteijn, F. Complexity behind CO_2 Capture on NH_2-MIL-53(Al). *Langmuir* **2011**, *27*, 3970. (b) Krap, C. P.; Newby, R.; Dhakshinamoorthy, A.; Garcia, H.; Cebula, I.; Easun, T. L.; Savage, M.; Eyley, J. E.; Gao, S.; Blake, A. J.; Lewis, W.; Beton, P. H.; Warren, M. R.; Allan, D. R.; Frogley, M. D.; Tang, C. C.; Cinque, G.; Yang, S.; Schröder, M. Enhancement of CO_2 adsorption and catalytic properties by Fe-doping of $[Ga_2(OH)_2(L)]$ (H_4L = biphenyl-3,3′,5,5′-tetracarboxylic acid), MFM-300(Ga_2). *Inorg. Chem.* **2016**, *55*, 1076. (c) Greenaway, A.; Gonzalez-Santiago, B.; Donaldson, P. M.; Frogley, M. D.; Cinque, G.; Sotelo, J.; Moggach, S.; Shiko, E.; Brandani, S.; Howe, R. F.; Wright, P. A. In situ synchrotron IR microspectroscopy of CO_2 adsorption on single crystals of the functionalized MOF Sc_2(BDC-NH_2)$_3$. *Angew. Chem., Int. Ed.* **2014**, *53*, 13483.

(18) (a) Supronowicz, B.; Mavrandonakis, A.; Heine, T. Interaction of small gases with the unsaturated metal centers of the HKUST-1 metal organic framework. *J. Phys. Chem. C* **2013**, *117*, 14570. (b) Grajciar, L.; Wiersum, A. D.; Llewellyn, P. L.; Chang, J.-S.; Nachtigall, P. Understanding CO_2 adsorption in CuBTC MOF: comparing combined DFT-ab initio calculations with microcalorimetry experiments. *J. Phys. Chem. C* **2011**, *115*, 17925. (c) Grajciar, L.; Nachtigall, P.; Bludský, O.; Rubeš, M. Accurate ab initio description of adsorption on coordinatively unsaturated Cu^{2+} and Fe^{3+} sites in MOFs. *J. Chem. Theory Comput.* **2015**, *11*, 230. (d) Lorzing, G. R.; Gosselin, E. J.; Trump, B. A.; York, A. H. P.; Sturluson, A.; Rowland, C. A.; Yap, G. P. A.; Brown, C. M.; Simon, C. M.; Bloch, E. D. Understanding gas storage in cuboctahedral porous coordination cages. *J. Am. Chem. Soc.* **2019**, *141*, 12128.

(19) (a) Sumida, K.; Rogow, D. L.; Mason, J. A.; McDonald, T. M.; Bloch, E. D.; Herm, Z. R.; Bae, T.-H.; Long, J. R. Carbon dioxide capture in metal-organic frameworks. *Chem. Rev.* **2012**, *112*, 724. (b) Nugent, P.; Belmabkhout, Y.; Burd, S. D.; Cairns, A. J.; Luebke, R.; Forrest, K.; Pham, T.; Ma, S.; Space, B.; Wojtas, L.; Eddaoudi, M.; Zaworotko, M. J. Porous materials with optimal adsorption thermodynamics and kinetics for CO_2 separation. *Nature* **2013**, *495*, 80.

(20) Chaemchuen, S.; Kabir, N. A.; Zhou, K.; Verpoort, F. Metal-organic frameworks for upgrading biogas via CO_2 adsorption to biogas green energy. *Chem. Soc. Rev.* **2013**, *42*, 9304.

(21) (a) Evans, J. D.; Sumby, C. J.; Doonan, C. J. Post-synthetic metalation of metal-organic frameworks. *Chem. Soc. Rev.* **2014**, *43*, 5933. (b) Das, A.; D'Alessandro, D. M. Tuning the functional sites in

metal-organic frameworks to modulate CO_2 heats of adsorption. *CrystEngComm* **2015**, *17*, 706.

(22) (a) Sharma, N.; Dhankhar, S. S.; Kumar, S.; Kumar, T. J. D.; Nagaraja, C. M. Rational design of a 3D Mn^{II}-metal−organic framework based on a nonmetallated porphyrin linker for selective capture of CO_2 and one-pot synthesis of styrene carbonates. *Chem. - Eur. J.* **2018**, *24*, 16662. (b) Singh Dhankhar, S.; Sharma, N.; Kumar, S.; Dhilip Kumar, T. J.; Nagaraja, C. M. rational design of a bifunctional, two-fold interpenetrated Zn^{II}-metal−organic framework for selective adsorption of CO_2 and efficient aqueous phase sensing of 2,4,6-trinitrophenol. *Chem. - Eur. J.* **2017**, *23*, 16204−16212.

(23) Alsmail, N. H.; Suyetin, M.; Yan, Y.; Cabot, R.; Krap, C. P.; Lu, J.; Easun, T. L.; Bichoutskaia, E.; Lewis, W.; Blake, A. J.; Schröder, M. Analysis of high and selective uptake of CO_2 in an oxamide-containing $\{Cu_2(OOCR)_4\}$-based metal-organic framework. *Chem. - Eur. J.* **2014**, *20*, 7317.

(24) Yang, S.; Sun, J.; Ramirez-Cuesta, A. J.; Callear, S. K.; David, W. I.; Anderson, D. P.; Newby, R.; Blake, A. J.; Parker, J. E.; Tang, C. C.; Schröder, M. Selectivity and direct visualization of carbon dioxide and sulfur dioxide in a decorated porous host. *Nat. Chem.* **2012**, *4*, 887.

(25) (a) Yu, J.; Wu, Y.; Balbuena, P. B. Response of metal sites toward water effects on postcombustion CO_2 capture in metal-organic frameworks. *ACS Sustainable Chem. Eng.* **2016**, *4*, 2387. (b) Nguyen, N. T. T.; Lo, T. N. H.; Kim, J.; Nguyen, H. T. D.; Le, T. B.; Cordova, K. E.; Furukawa, H. Mixed-metal zeolitic imidazolate frameworks and their selective capture of wet carbon dioxide over methane. *Inorg. Chem.* **2016**, *55*, 6201. (c) Kim, D.; Lim, H.-K.; Ro, H.; Kim, H.; Lee, H. Unexpected carbon dioxide inclusion in water-saturated pores of metal-organic frameworks with potential for highly selective capture of CO_2. *Chem. - Eur. J.* **2015**, *21*, 1125.

(26) Cooper, A. I.; Poliakoff, M. High-pressure reactions in polyethylene films, a new development in matrix isolation. The photochemical reaction of iron pentacarbonyl with nitrogen and the thermal reaction of iron tetracarbonyl dinitrogen $[Fe(CO)_4(N_2)]$ with hydrogen. *Chem. Phys. Lett.* **1993**, *212*, 611.

(27) Nowell, H.; Barnett, S. A.; Christensen, K. E.; Teat, S. J.; Allan, D. R. I19, the small-molecule single-crystal diffraction beamline at Diamond Light Source. *J. Synchrotron Radiat.* **2012**, *19*, 435.

(28) *CrystalClear*; Rigaku MSC: 491 South Orem Blvd, Orem, UT 84058, USA, 2010.

(29) Sheldrick, G. Crystal structure refinement with SHELXL. *Acta Crystallogr., Sect. C: Struct. Chem.* **2015**, *71*, 3.

(30) Spek, A. PLATON SQUEEZE: a tool for the calculation of the disordered solvent contribution to the calculated structure factors. *Acta Crystallogr., Sect. C: Struct. Chem.* **2015**, *71*, 9.

(31) *CrysAlis PRO*; Agilent Technologies: Yarnton, Oxfordshire, England, 2014.

(32) Chapon, L. C.; Manuel, P.; Radaelli, P. G.; Benson, C.; Perrott, L.; Ansell, S.; Rhodes, N. J.; Raspino, D.; Duxbury, D.; Spill, E.; Norris, J. Wish: The new powder and single crystal magnetic diffractometer on the second target station. *Neutron News* **2011**, *22*, 22.

(33) Shao, Y.; Gan, Z.; Epifanovsky, E.; Gilbert, A. T. B.; Wormit, M.; Kussmann, J.; Lange, A. W.; Behn, A.; Deng, J.; Feng, X.; Ghosh, D.; Goldey, M.; Horn, P. R.; Jacobson, L. D.; Kaliman, I.; Khaliullin, R. Z.; Kuś, T.; Landau, A.; Liu, J.; Proynov, E. I.; Rhee, Y. M.; Richard, R. M.; Rohrdanz, M. A.; Steele, R. P.; Sundstrom, E. J.; Woodcock, H. L.; Zimmerman, P. M.; Zuev, D.; Albrecht, B.; Alguire, E.; Austin, B.; Beran, G. J. O.; Bernard, Y. A.; Berquist, E.; Brandhorst, K.; Bravaya, K. B.; Brown, S. T.; Casanova, D.; Chang, C.-M.; Chen, Y.; Chien, S. H.; Closser, K. D.; Crittenden, D. L.; Diedenhofen, M.; DiStasio, R. A.; Do, H.; Dutoi, A. D.; Edgar, R. G.; Fatehi, S.; Fusti-Molnar, L.; Ghysels, A.; Golubeva-Zadorozhnaya, A.; Gomes, J.; Hanson-Heine, M. W. D.; Harbach, P. H. P.; Hauser, A. W.; Hohenstein, E. G.; Holden, Z. C.; Jagau, T.-C.; Ji, H.; Kaduk, B.; Khistyaev, K.; Kim, J.; Kim, J.; King, R. A.; Klunzinger, P.; Kosenkov, D.; Kowalczyk, T.; Krauter, C. M.; Lao, K. U.; Laurent, A. D.; Lawler, K. V.; Levchenko, S. V.; Lin, C. Y.; Liu, F.; Livshits, E.; Lochan, R. C.; Luenser, A.; Manohar, P.; Manzer, S. F.; Mao, S.-P.; Mardirossian, N.; Marenich, A. V.; Maurer, S. A.; Mayhall, N. J.; Neuscamman, E.; Oana, C. M.; Olivares-Amaya, R.; O'Neill, D. P.; Parkhill, J. A.; Perrine, T. M.; Peverati, R.; Prociuk, A.; Rehn, D. R.; Rosta, E.; Russ, N. J.; Sharada, S. M.; Sharma, S.; Small, D. W.; Sodt, A. Advances in molecular quantum chemistry contained in the Q-Chem 4 program package. *Mol. Phys.* **2015**, *113*, 184.

(34) Grimme, S.; Antony, J.; Ehrlich, S.; Krieg, H. A consistent and accurate ab initio parametrization of density functional dispersion correction (DFT-D) for the 94 elements H-Pu. *J. Chem. Phys.* **2010**, *132*, 154104.

(35) Mitin, A. V.; Baker, J.; Pulay, P. An improved 6-31G* basis set for first-row transition metals. *J. Chem. Phys.* **2003**, *118*, 7775.

(36) Boys, S. F.; Bernardi, F. The calculation of small molecular interactions by the differences of separate total energies. Some procedures with reduced errors. *Mol. Phys.* **1970**, *19*, 553.

(37) (a) Prakash, M. J.; Zou, Y.; Hong, S.; Park, M.; Bui, M.-P. N.; Seong, G. H.; Lah, M. S. Metal-organic polyhedron based on a Cu^{II} paddle-wheel secondary building unit at the truncated octahedron corners. *Inorg. Chem.* **2009**, *48*, 1281. (b) Chen, Z.; Liu, X.; Wu, A.; Liang, Y.; Wang, X.; Liang, F. Synthesis, structure and properties of an octahedral dinuclear-based Cu_{12} nanocage of trimesoyltri(l-alanine). *RSC Adv.* **2016**, *6*, 9911. (c) Zhu, H.-F.; Fan, J.; Okamura, T.-A.; Zhang, Z.-H.; Liu, G.-X.; Yu, K.-B.; Sun, W.-Y.; Ueyama, N. Metal-organic architectures of silver(I), cadmium(II), and copper(II) with a flexible tricarboxylate ligand. *Inorg. Chem.* **2006**, *45*, 3941.

(38) Pan, M.; Wu, K.; Zhang, J.-H.; Su, C.-Y. Chiral metal−organic cages/containers (MOCs): From structural and stereochemical design to applications. *Coord. Chem. Rev.* **2019**, *378*, 333.

(39) (a) Sokolowski, K.; Bury, W.; Justyniak, I.; Fairen-Jimenez, D.; Soltys, K.; Prochowicz, D.; Yang, S.; Schröder, M.; Lewinski, J. Permanent porosity derived from the self-assembly of highly luminescent molecular zinc carbonate nanoclusters. *Angew. Chem., Int. Ed.* **2013**, *52*, 13414. (b) Ni, Z.; Yassar, A.; Antoun, T.; Yaghi, O. M. Porous metal-organic truncated octahedron constructed from paddle-wheel squares and terthiophene Links. *J. Am. Chem. Soc.* **2005**, *127*, 12752. (c) Furukawa, H.; Kim, J.; Ockwig, N. W.; O'Keeffe, M.; Yaghi, O. M. Control of vertex geometry, structure dimensionality, functionality, and pore metrics in the reticular synthesis of crystalline metal-organic frameworks and polyhedra. *J. Am. Chem. Soc.* **2008**, *130*, 11650. (d) Gosselin, E. J.; Rowland, C. A.; Bloch, E. D. Permanently microporous metal−organic polyhedra. *Chem. Rev.* **2020**, DOI: 10.1021/acs.chemrev.9b00803.

(40) Spackman, M. A.; Jayatilaka, D. Hirshfeld surface analysis. *CrystEngComm* **2009**, *11*, 19.

(41) (a) Ye, Y.; Xiong, S.; Wu, X.; Zhang, L.; Li, Z.; Wang, L.; Ma, X.; Chen, Q.-H.; Zhang, Z.; Xiang, S. Microporous metal-organic framework stabilized by balanced multiple host-counteranion hydrogen-bonding interactions for high-density CO_2 capture at ambient conditions. *Inorg. Chem.* **2016**, *55*, 292. (b) Craig, G. A.; Larpent, P.; Urabe, H.; Legrand, A.; Bonneau, M.; Kusaka, S.; Furukawa, S. Hysteresis in the gas sorption isotherms of metal−organic cages accompanied by subtle changes in molecular packing. *Chem. Commun.* **2020**, *56*, 3689.

(42) Liu, G.; Di Yuan, Y.; Wang, J.; Cheng, Y.; Peh, S. B.; Wang, Y.; Qian, Y.; Dong, J.; Yuan, D.; Zhao, D. Process-tracing study on the postassembly modification of highly stable zirconium metal-organic cages. *J. Am. Chem. Soc.* **2018**, *140*, 6231.

(43) (a) Todaro, M.; Buscarino, G.; Sciortino, L.; Alessi, A.; Messina, F.; Taddei, M.; Ranocchiari, M.; Cannas, M.; Gelardi, F. M. Decomposition process of carboxylate MOF HKUST-1 unveiled at the atomic scale level. *J. Phys. Chem. C* **2016**, *120*, 12879. (b) Soubeyrand-Lenoir, E.; Vagner, C.; Yoon, J. W.; Bazin, P.; Ragon, F.; Hwang, Y. K.; Serre, C.; Chang, J.-S.; Llewellyn, P. L. How water fosters a remarkable 5-fold increase in low-pressure CO_2 uptake within mesoporous MIL-100(Fe). *J. Am. Chem. Soc.* **2012**, *134*, 10174. (c) Burtch, N. C.; Jasuja, H.; Walton, K. S. Water stability and adsorption in metal-organic frameworks. *Chem. Rev.* **2014**, *114*, 10575. (d) Mollick, S.; Mukherjee, S.; Kim, D.; Qiao, Z.; Desai, A. V.; Saha, R.; More, Y. D.; Jiang, J.; Lah, M. S.; Ghosh, S. K. Hydrophobic

shielding of outer surface: enhancing the chemical stability of metal−organic polyhedra. *Angew. Chem., Int. Ed.* **2019**, *58*, 1041.

(44) Malkmus, W. Infrared emissivity of carbon dioxide (2.7-μ band). *J. Opt. Soc. Am.* **1964**, *54*, 751.

(45) (a) Vimont, A.; Travert, A.; Bazin, P.; Lavalley, J.-C.; Daturi, M.; Serre, C.; Ferey, G.; Bourrelly, S.; Llewellyn, P. L. Evidence of CO_2 molecule acting as an electron acceptor on a nanoporous metal-organic-framework MIL-53 or $Cr^{3+}(OH)(O_2C-C_6H_4-CO_2)$. *Chem. Commun.* **2007**, 3291. (b) Yang, W.; Davies, A. J.; Lin, X.; Suyetin, M.; Matsuda, R.; Blake, A. J.; Wilson, C.; Lewis, W.; Parker, J. E.; Tang, C. C.; George, M. W.; Hubberstey, P.; Kitagawa, S.; Sakamoto, H.; Bichoutskaia, E.; Champness, N. R.; Yang, S.; Schröder, M. Selective CO_2 uptake and inverse CO_2/C_2H_2 selectivity in a dynamic bifunctional metal-organic framework. *Chem. Sci.* **2012**, *3*, 2993.

(46) (a) Wriedt, M.; Sculley, J. P.; Yakovenko, A. A.; Ma, Y.; Halder, G. J.; Balbuena, P. B.; Zhou, H.-C. Low-energy selective capture of carbon dioxide by a pre-designed elastic single-molecule trap. *Angew. Chem., Int. Ed.* **2012**, *51*, 9804. (b) Cui, P.; Ma, Y.-G.; Li, H.-H.; Zhao, B.; Li, J.-R.; Cheng, P.; Balbuena, P. B.; Zhou, H.-C. Multipoint interactions enhanced CO_2 uptake: a zeolite-like zinc-tetrazole framework with 24-nuclear zinc cages. *J. Am. Chem. Soc.* **2012**, *134*, 18892.

(47) Prokhvatilov, A. I.; Isakina, A. P. An X-ray powder diffraction study of crystalline α-methane-d$_4$. *Acta Crystallogr., Sect. B: Struct. Crystallogr. Cryst. Chem.* **1980**, *36*, 1576.

(48) Webster, C. E.; Drago, R. S.; Zerner, M. C. Molecular dimensions for adsorptives. *J. Am. Chem. Soc.* **1998**, *120*, 5509.

(49) Mecozzi, S.; Rebek, J., Jr. The 55% solution: a formula for molecular recognition in the liquid state. *Chem. - Eur. J.* **1998**, *4*, 1016.